Conservative Finite Element Modeling of EEG and MEG on Unstructured Grids

N. Yavich, N. Koshev, M. Malovichko, A. Razorenova, M. Fedorov

Abstract—**For interpretation of electroencephalography (EEG) and magnetoencephalography (MEG) data, multiple solutions of the respective forward problems are needed. In this paper, we assess performance of the mixed-hybrid finite element method (MHFEM) applied to EEG and MEG modeling. The method provides an approximate potential and induced currents and results in a system with a positive semi-definite matrix. The system thus can be solved with a variety of standard methods (e.g. the preconditioned conjugate gradient method). The induced currents satisfy discrete charge conservation law making the method conservative. We studied its performance on unstructured tetrahedral grids for a layered spherical head model as well as a realistic head model. We also compared its accuracy versus the conventional nodal finite element method (P_1 FEM). To avoid modeling singular sources, we completed our computations with a subtraction approach; the derived expression for the MEG response different from earlier published and involves integration of finite quantities only. We conclude that although the MHFEM is more computationally demanding than the P_1 FEM, its use is justified for EEG and MEG modeling on low-resolution head models where P_1 FEM loses accuracy.**

Index Terms—**EEG, MEG, forward problem, unstructured grids, mixed-hybrid finite element method, subtraction approach.**

I. INTRODUCTION

Electroencephalography (EEG) and magnetoencephalography (MEG) are two noninvasive modalities to investigate living brain activity. They feature excellent temporal resolution and thus are commonly applied in clinical and experimental settings.

Accurate interpretation of EEG and MEG data requires multiple solutions of the forward problem, which describes propagation of the neural currents within the head volume conductor. The quasi-static mode of Maxwell's equations is typically assumed [1].

The forward problem seeks a response due to a single cortical dipole. Numerical methods are needed to solve these equations for anatomical head models, typically resulting from MRI followed by segmentation of the scans. However, numerical modeling is complicated by the complex geometry of the head tissues as well as by their conductivity inhomogeneity and possibly anisotropy, and source singularity.

Conventional (i.e. Lagrange P_1 nodal) finite-element method (FEM) modeling is used for several decades for EEG modeling (e.g. [2], [3]) due to excellent geometrical flexibility needed for anatomical head modeling. The method also results in a symmetric positive semi-definite system of equations, making many solvers applicable [4]. On the other hand, two fundamental limitations of the method should be noted. Firstly, conventional FEM disregards the charge conservation law what in some cases (e.g. highly localized sources or heterogeneous problems) results in inaccurate responses. Secondly, the MEG response when computed via Biot-Savart's law, depends on the gradient of the potential. However, the gradient has a slower convergence, i.e. found less accurate than the potential. This overall results in a less accurate MEG response. Alternatively, the Geselowitz formula [1] can be used to compute MEG data, but it still cannot be applied when conductivity is anisotropic or organ surfaces are not closed, e.g. the fontanel in the skull of human neonates.

The finite-volume method (FVM) [5], is known to be conservative and results in a positive semi-definite system matrix. Another known alternative is the discontinuous Galerkin (DG) FEM method which resolves the issue of violation of charge conservation (see e.g. [6]–[8]).

Mixed FEM [9] explicitly enforces charge conservation and thus is attractive for heterogeneous problems like head volume conductor modeling. The method features computation of both solution and its normal flux. In this case, the integrated charge conservation law is directly enforced over each element. However, its main disadvantage is that the resulting system of equations has an indefinite matrix since the problem has a saddle-point structure. This is inconvenient for practical use of mixed FEM schemes, though the system can be solved with the Uzawa algorithm [10].

There is a technique called *hybridization* which introduces extra unknowns (interelement multipliers) to the mixed FEM formulation. After simple manipulations, the extended system can be reduced to a positive semi-definite one and thus can be solved with a variety of standard methods. We thus see that mixed hybrid FEM (MHFEM) combines many benefits compared to its competitors.

An application of the mixed FEM to EEG modeling on structured cubic grids was presented in [11]. In our work, we focus on the use of unstructured tetrahedral grids for EEG and MEG modeling. We also present and assess a hybridization technique as well as introduce a subtraction approach for the

N. Yavich and M. Malovichko are with Skolkovo Institute of Science and Technology, Moscow, 121205 Russia and also with Moscow Institute of Physics and Technology, Dolgoprudny, 141701 Russia (e-mail: N.Yavich@skoltech.ru).

N. Koshev and A. Razorenova are with Skolkovo Institute of Science and Technology, Moscow, 121205 Russia

M. Fedorov is with Sirius University of Science and Technology, Sochi, 354340, Russia and also with Skolkovo Institute of Science and Technology, Moscow, 121205 Russia

mixed FEM. As far as the authors are concerned, none of these topics were earlier discussed for EEG and MEG modeling.

II. EEG/MEG FORWARD PROBLEM

Neural currents recorded by EEG and MEG sensors are of relatively low frequency, from 0.1 to 100 Hz. In this frequency range, signal propagation within the heterogeneous head volume conductor Ω is governed by the diffusion equation for the potential p, completed by Neumann boundary conditions on the conductor boundary Γ,

$$-div(\sigma\nabla p) = -div\ \boldsymbol{J} \text{ in } \Omega,$$
$$\sigma\nabla p \cdot \boldsymbol{\nu} = 0 \text{ on } \Gamma. \tag{1}$$

Here, $\boldsymbol{J}$ is source current density, σ is conductivity and $\boldsymbol{\nu}$ is the unit outward normal to Γ. The potential p is known to be defined up to an additive constant. Each head organ is expected to have constant conductivity σ_i, $i = 1\cdots N$. The surfaces separating different organs are denoted as S_j, $j = 1\cdots M$.

The magnetic induction, $\boldsymbol{B}$, is formed by the primary, $\boldsymbol{B}_p(\boldsymbol{r})$, and secondary, $\boldsymbol{B}_s(\boldsymbol{r})$, terms,

$$\boldsymbol{B}(\boldsymbol{r}) = \boldsymbol{B}_p(\boldsymbol{r}) + \boldsymbol{B}_s(\boldsymbol{r}). \tag{2}$$

For a dipole source, $\boldsymbol{B}_p(\boldsymbol{r})$ is found analytically, while $\boldsymbol{B}_s(\boldsymbol{r})$ can be found via the Biot-Savart's law,

$$\boldsymbol{B}_s(\boldsymbol{r}) = -\frac{\mu_0}{4\pi}\int_\Omega \sigma\nabla p(\boldsymbol{r}') \times \frac{\boldsymbol{r} - \boldsymbol{r}'}{|\boldsymbol{r} - \boldsymbol{r}'|^3} dV'. \tag{3}$$

We emphasize that Biot-Savart's law involve volume integration, what results in high computational complexity of the expression for $\boldsymbol{B}_s(r)$. Alternatively, the secondary magnetic induction can be expressed through surface integrals (Geselowitz formula, [1]),

$$\boldsymbol{B}_s(\boldsymbol{r}) = \frac{\mu_0}{4\pi}\sum_{j=1}^{M}(\sigma'_j - \sigma''_j)\int_{S_j} p(\boldsymbol{r}')\frac{\boldsymbol{r} - \boldsymbol{r}'}{|\boldsymbol{r} - \boldsymbol{r}'|^3} \times \boldsymbol{\nu} dS', \tag{4}$$

where $\boldsymbol{\nu}$ is a unit normal to S_j and directed from a subdomain with conductivity σ'_j to a subdomain with conductivity σ''_j.

III. MODELING METHODS

Mixed methods are based on a reformulation of a second-order equation to two first-order equations. Notice that the second-order equation (1) can be transformed in at least two ways. The first is quite traditional for general diffusion problems [9],

$$\frac{1}{\sigma}\boldsymbol{w} + \nabla p = 0,$$
$$-div\ \boldsymbol{w} = div\ \boldsymbol{J}. \tag{5}$$

while the second looks attractive for direct current modeling, [11],

$$\frac{1}{\sigma}\boldsymbol{u} + \nabla p = \frac{1}{\sigma}\boldsymbol{J},$$
$$-div\ \boldsymbol{u} = 0. \tag{6}$$

Both formulations are completed with homogeneous Neumann boundary conditions.

We will continue with the second formulation since it avoids differentiation of the source current density. In this formulation, $\boldsymbol{u} = \boldsymbol{J} - \sigma\nabla p$ corresponds to induced currents. Neural sources modeling involves incorporation of dipole sources (equivalent current dipole notion, [12]). To avoid direct incorporation of dipole sources, we combined (6) with the subtraction method, Appendix C. In other applications, this method is also referred as singularly removal, [13]. It basically substitutes $\boldsymbol{J}$ with the secondary source as well as substitutes homogeneous Neumann boundary condition with inhomogeneous. Nevertheless, to make the presentation clearer, we still follow the notations of (6).

Let us now introduce mixed-hybrid approximation to (6). Define $\mathfrak{T}_h = \{V_1 \cdots V_n\}$ to be regular partitioning of Ω into n tetrahedrons, and γ_{sr} be the face between tetrahedrons V_s and V_r, $1 \le s, r \le n$. We further denote as $\mathcal{F}_h$ the set of all the faces and their total number as m.

Multiply the first equation in (6) with an arbitrary vector field v, and the second equation with an arbitrary scalar field q. Integration over a tetrahedron V_s results in the following identities,

$$\int_{V_s}\frac{1}{\sigma}\boldsymbol{u}\cdot\boldsymbol{v}dV + \int_{V_s}\nabla p\cdot\boldsymbol{v}dV = \int_{V_s}\frac{1}{\sigma}\boldsymbol{J}\cdot\boldsymbol{v}dV,$$
$$-\int_{V_s} q\ div\ \boldsymbol{u}dV = 0. \tag{7}$$

Applying Green's identity and divergence theorem to the second term in the first equation, we receive,

$$\int_{V_s}\frac{1}{\sigma}\boldsymbol{u}\cdot\boldsymbol{v}dV - \int_{V_s} p\ div\ \boldsymbol{v}dV + \int_{\partial V_s} p\ \boldsymbol{v}\cdot\boldsymbol{\nu}dS = \int_{V_s}\frac{1}{\sigma}\boldsymbol{J}\cdot\boldsymbol{v}dV. \tag{8}$$

Denote as λ values of the potential on the grid faces, i.e. if $\gamma_{sr} \in \mathcal{F}_h$ is some face between tetrahedron s and tetrahedron r, then $\lambda(\boldsymbol{r}) = p(\boldsymbol{r})$ for $\boldsymbol{r} \in \gamma_{sr}$.

We make use of the standard notation for the space of square-integrable functions over the modeling domain, $L_2(\Omega)$, and over faces, $L_2(\mathcal{F}_h)$. The space $H(div, \Omega)$ consists of L_2 vector fields with divergence in L_2. Also define

$$U = \{\boldsymbol{v} \in L_2(\Omega), \quad \boldsymbol{v}|_{V_s} \in H(div, V_s)\},$$
$$Q = L_2(\Omega), \tag{9}$$
$$\Lambda = \{\mu \in L_2(\mathcal{F}_h), \quad \mu|_{\gamma_{sr}} \in L_2(\gamma_{sr}), \gamma_{sr} \in \mathcal{F}_h\}.$$

Note that vector fields from U might be discontinuous across the element interfaces. Summing up the identities over tetrahedrons, we arrive to mixed-hybrid formulation: find $(\boldsymbol{u}, p, \lambda) \in U \times Q \times \Lambda$ such that

$$\int_\Omega\frac{1}{\sigma}\boldsymbol{u}\cdot\boldsymbol{v}dV - \int_\Omega p\ div\ \boldsymbol{v}dV$$
$$+ \sum_{s=1}^{n}\int_{\partial V_s}\lambda\ \boldsymbol{v}\cdot\boldsymbol{\nu}dS = \int_\Omega\frac{1}{\sigma}\boldsymbol{J}\cdot\boldsymbol{v}dV,$$
$$-\int_\Omega q\ div\ \boldsymbol{u}dV = 0. \tag{10}$$
$$\sum_{1\le s<t\le n}\int_{\gamma_{st}}\mu(\boldsymbol{u}^s - \boldsymbol{u}^t)\cdot\boldsymbol{\nu}dS = 0.$$

for all $(\boldsymbol{v}, q, \mu) \in U \times Q \times \Lambda$. The third set of equations enforces continuity of the normal component of the induced

currents as well as fulfillment of the Neumann boundary condition. Consequently, in this formulation, components of λ are commonly referred to as interelement or Lagrange multipliers.

For finite-element solution of (10), define the following finite-dimensional subspaces,

$$
\begin{aligned}
U_h &= \{\boldsymbol{v}_h \in L_2(\Omega), \quad \boldsymbol{v}_h|_{V_s} \in RT_0(V_s)\}, \\
Q_h &= \{q_h \in L_2(\Omega), \quad q_h|_{V_s} \in P_0(V_s)\}, \\
\Lambda_h &= \{\mu_h \in L_2(\mathcal{F}_h), \quad \mu_h|_{\gamma_{sr}} \in P_0(\gamma_{sr}), \gamma_{sr} \in \mathcal{F}_h\}.
\end{aligned}
\tag{11}
$$

where $P_0(V_s)$ and $P_0(\gamma_{sr})$ are the spaces of constant functions of a tetrahedron or face, respectively; $RT_0(V_s)$ is the lowest-order Raviart-Thomas space of affine vector functions, [14]. Higher-order approximations could be considered in a similar way. Also note that continuity of vector fields from U_h is relaxed. Now the finite-dimensional counterpart is as follows: find $(\boldsymbol{u}_h, p_h, \lambda_h) \in U_h \times Q_h \times \Lambda_h$ such that

$$
\begin{aligned}
\int_\Omega \frac{1}{\sigma} \boldsymbol{u}_h \cdot \boldsymbol{v}_h dV &- \int_\Omega p_h\ div\ \boldsymbol{v}_h dV + \\
\sum_{s=1}^n \int_{\partial V_s} \lambda_h\ \boldsymbol{v}_h \cdot \boldsymbol{\nu} dS &= \int_\Omega \frac{1}{\sigma} \boldsymbol{J} \cdot \boldsymbol{v}_h dV, \\
&- \int_\Omega q_h\ div\ \boldsymbol{u}_h dV = 0, \\
\sum_{1 \le s < t \le n} \int_{\gamma_{st}} \mu_h(\boldsymbol{u}_h^s - \boldsymbol{u}_h^t) \cdot \nu dS &= 0.
\end{aligned}
\tag{12}
$$

for all $(\boldsymbol{v}_h, q_h, \mu_h) \in U_h \times Q_h \times \Lambda_h$.

The resulting system of linear equation has the following form,

$$
\begin{pmatrix} A & -B & C \\ -B^T & 0 & 0 \\ C^T & 0 & 0 \end{pmatrix} \begin{pmatrix} \boldsymbol{u}_h \\ p_h \\ \lambda_h \end{pmatrix} = \begin{pmatrix} f_h \\ 0 \\ 0 \end{pmatrix}.
\tag{13}
$$

Entries of the system matrix and right-hand side are expressed through the basis function of (11). Let $\boldsymbol{v}_i, i = 1 \cdots 4n$, $q_s, s = 1 \cdots n$, and $\mu_k, k = 1 \cdots m$ be the basis functions of U_h, Q_h and Λ_h, respectively. We then can write,

$$
A_{ij} = \int_\Omega \frac{1}{\sigma} \boldsymbol{v}_i \cdot \boldsymbol{v}_j dV, \quad B_{sj} = \int_\Omega q_s\ div\ \boldsymbol{v}_j dV,
$$

$$
C_{ik} = \int_{\gamma_i} \mu_k(\boldsymbol{v}_i - \boldsymbol{v}_{i'}) \cdot \nu dS, \quad f_i = \int_\Omega \frac{1}{\sigma} \boldsymbol{J} \cdot \boldsymbol{v}_i dV,
$$

where $\boldsymbol{v}_i$ and $\boldsymbol{v}_{i'}$ are two basis functions in the two tetrahedrons sharing face γ_i and corresponding to degree of freedom on this face.

We would like to emphasize that the second equation of (6) enforces the charge conservation law. This equation is then directly involved in (7) and (12), (13). Consequently, the numerical induced current, $\boldsymbol{u}_h$, satisfies this equation within every tetrahedron with machine precision, given we solved (12) exactly.

The mixed finite element system, [9], has size $n + m$ and a somewhat similar block structure. However, several important differences should be emphasized. The size of (13) is $5n + m$, i.e. the hybridized system is actually larger. In Appendix A, we describe a procedure to elegantly eliminate $\boldsymbol{u}_h$ and p_h from

this system and receive a system for interelement multipliers only,

$$
S \lambda_h = g_h.
\tag{14}
$$

This system has a sparse symmetric positive semi-definite matrix and its size is equal to the number of faces, m. Consequently, for this system, an efficient solver is straightforward to construct, e.g. the conjugate gradient method with an AMG preconditioner, for example [15].

After λ_h is found, the potential p_h and induced currents $\boldsymbol{u}_h$ can be recovered. To summarize, we described a conservative finite-element scheme which requires $O(m \log(1/\varepsilon))$ arithmetical operations for a single solution, where ε is the desired tolerance. Elimination and recovery of p_h and $\boldsymbol{u}_h$ take linear time.

When induced currents are found, the magnetic flux is computed via (3),

$$
\boldsymbol{B}(\boldsymbol{r}) = \frac{\mu_0}{4\pi} \int_\Omega \boldsymbol{u}(\boldsymbol{r}') \times \frac{\boldsymbol{r} - \boldsymbol{r}'}{|\boldsymbol{r} - \boldsymbol{r}'|^3} dV'.
\tag{15}
$$

Alternatively, since the MHFEM provides an approximation for face-centered potential values, λ, we can exploit them in the Geselowitz formula and obtain the secondary magnetic induction, $\boldsymbol{B}_s(r)$,

$$
\boldsymbol{B}_s(\boldsymbol{r}) = \frac{\mu_0}{4\pi} \sum_{j=1}^M (\sigma_j' - \sigma_j'') \int_{S_j} \lambda(\boldsymbol{r}') \frac{\boldsymbol{r} - \boldsymbol{r}'}{|\boldsymbol{r} - \boldsymbol{r}'|^3} \times \boldsymbol{\nu} dS'.
\tag{16}
$$

We will examine both options in the next section.

For dipole source modeling, we represented (3) and (15) so that they would involve integration of finite quantities only (Appendix B and C).

IV. MODELING EXAMPLES

In this section, we discuss implementation details as well as present and analyze the results of numerical modeling of the described above mixed-hybrid FEM for layered spherical and real head models.

A. Implementation

We implemented the mixed-hybrid FEM for EEG and MEG data modeling on unstructured tetrahedral grids. Our implementation was in C++ and used the `Modular FEM` library [16]. The large sparse linear system (14) was solved with the conjugate gradient method leveraged by the `BoomerAMG` preconditioner, [15], and solver tolerance, ε, was set to 10^{-10}. All the integrations were performed with the second-order quadratures. For a comparison purpose, we also implemented the conventional P_1 FEM. Both FEMs were completed with the subtraction method to avoid modeling source singularity (Appendices B and C).

B. EEG and MEG Data Modeling in a Layered Spherical Head

In this subsection, we modeled the EEG and MEG data within a layered spherical head. In this head model (Fig. 1.), the brain counterpart had 7.8 cm radius and conductivity 0.3
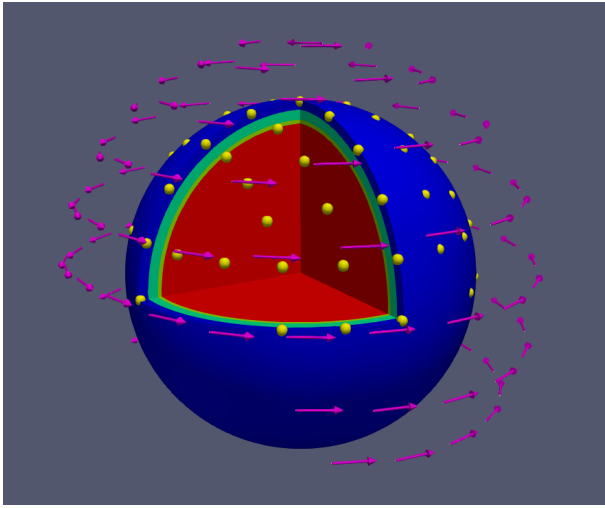
Fig. 1: Layered spherical head with the standard 10-10 EEG layout (yellow balls) and 102 tangential magnetometers (violet arrows). Color corresponds to different tissues: red – brain, yellow – CSF, turquoise – skull, blue – scalp.
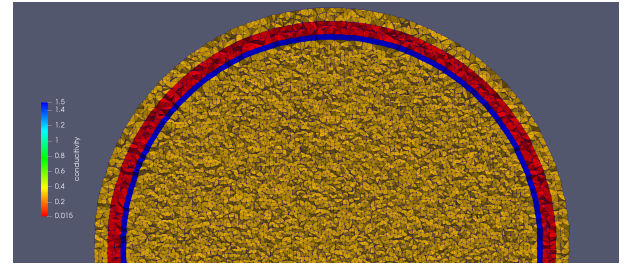

Fig. 2: The fine tetrahedral grid for the layered spherical head; color indicates conductivity, S/m
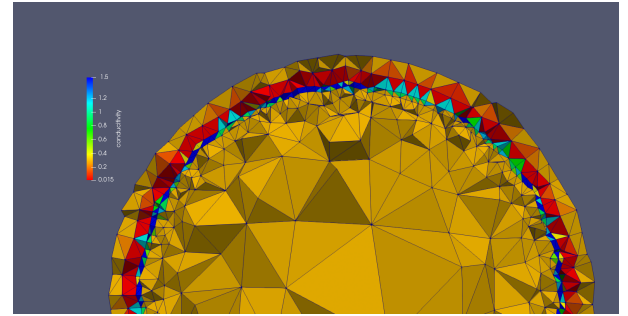

Fig. 3: The coarse tetrahedral grid for the layered spherical head; color indicates conductivity, S/m. Since the grid is not aligned with surfaces separating different tissues, conductivity values shown here were averaged over elements

S/m, the CSF had 8 cm radius and conductivity 1.5 S/m, the skull had 8.5 cm radius and conductivity 0.015 S/m, and the scalp had 9 cm and conductivity 0.3 S/m. This head model was gridded using `Iso2Mesh` [17] package. Three tetrahedral grids were prepared for our experiments below. One is fairly typical for finite-element EEG/MEG modeling (Fig. 2), yet with possibly an excessive resolution; it had 777'425 vertices, 9'877'505 faces, 4'927'680 tetrahedrons, the maximum edge length of 0.36 cm and the minimum of 0.06 cm. It will be referred to as the *fine* grid since the tetrahedrons are of relatively the same size. The second one was intentionally picked of fairly low resolution and not aligned with surfaces separating different tissues, Fig. 3. It mimics the situation when an MRI image had artifacts [18] and/or was segmented coarsely. We will refer this grid as *coarse*. It had 29'644 vertices, 350'800 faces, 174'289 tetrahedrons, the maximum edge length of 4.3 cm and the minimum of 0.1 cm. The third one was received a single uniform refinement of the coarse grid and will be referred to as the *refined* grid. Summary of grid parameters is presented in Table I.

We want to comment on our particular choice of the fine grid. In [4], it was shown that the subtraction approach achieves higher numerical accuracy if a mesh has a higher density towards tissue interfaces where the right-hand side is non-zero. Still, we used a relatively uniform grid because it is more convenient for examining the numerical solution convergence with respect to grid size. One can expect a theoretical order of convergence on a sequence of uniform grids. Another benefit of the uniform mesh resolution is that our results easier to reproduce since the grids are controlled by a single parameter. In a scenario where the goal is not algorithm design but an applied EEG modeling with the highest possible accuracy, the grids should be adapted to tissue interfaces.

We modeled EEG and MEG responses due to dipole sources. Dipoles were located at eight different eccentricities

(ratio of the distance from the head center to dipole to the brain counterpart radius) varying from 0.10 to 0.99 unevenly. The most eccentric source was thus 0.78 mm from the CSF counterpart. At every eccentricity, we modeled 15 randomly oriented dipoles. We thus solved 120 forward problems overall at every grid.

We verified the responses at 71 electrode locations (corresponding to the standard 10-10 layout) and 102 magnetometer locations (corresponding to Elekta Neuromag®TRIUX™ system), Fig. 1. The magnetometer locations were scaled so that they would locate 3 cm outside the head. Since the normal component of the secondary magnetic field vanishes for this head model, we verified one of the tangential components.

An analytical expression for the MEG response is fairly simple (see e.g. [1]) while the expression for the EEG response is more complex. Our numerical solution was compared versus analytical formula, [19], available in a public-domain implementation. P_1 FEM EEG response was compared versus MH-FEM response (potential obtained from (13) and (25)). Using P_1 and mixed-hybrid FEMs we computed MEG responses

TABLE I: Summary on the two tetrahedral grids used for the layered spherical head; n number of tetrahedrons, l number of vertices, m number of faces, h_{max} longest edge, h_{min} shortest edge

	n	l	m	h_{max}	h_{min}
fine	4'927'680	777'425	9'877'505	0.36 cm	0.06 cm
coarse	174'289	29'644	350'800	4.3 cm	0.1 cm
refined	1'394'312	235'798	2'797'512	2.1 cm	0.05 cm

with Biot-Savart (31),(36) and Geselowitz representations (32), (37).

Two error measured were used to analyze the error, RDM and MAG, estimating topography and magnitude errors, respectively,

$$RDM = \left\| \frac{d_{num}}{\|d_{num}\|} - \frac{d_{ana}}{\|d_{ana}\|} \right\|,$$
$$MAG = \left| 1 - \frac{\|d_{num}\|}{\|d_{ana}\|} \right|,$$

(17)

where d_{num} is the numerical solution at electrode or magnetometer locations and d_{ana} is the respective analytical solution, and $\| \cdot \|$ denotes the euclidean norm.

Figure 4 illustrates the RDM and MAG error boxplots of the EEG and MEG responses versus source eccentricity, modeled with the fine grid. For EEG data, MHFEM errors are mainly higher than those of P_1 FEM. This follows from convergence estimates. For the potential variable in the $L_2(\Omega)$ space, they are as follows: $O(h^2)$ for the P_1 approximation of the potential in the Lagrange FEM and $O(h)$ for the P_0 approximation of the potential in the mixed FEM and MHFEM. This is reflected in our EEG fine grid modeling results.

We observe that the EEG data errors tend to grow with eccentricity. This is common for the subtraction method, [20]. From MEG data errors, we see that the Biot-Savart formula is more accurate at higher eccentricities for both FEMs, while the Geselowitz formula loses accuracy; this is typical for BEM modeling, [21].

Figure 5 shows the results of modeling with the coarse grid. We observe here that the MHFEM is more accurate than P_1 FEM both for EEG and MEG modeling. We attribute this to the conservation property of the MHFEM which is critical to model induced currents on low-resolution grids. A similar effect was noticed in [8], [7] for hexahedral grid modeling and was referred to as *skull leakage*. Modeling with Geselowitz was not included in this test since the coarse grid is not fitted to the organ geometry.

Table II summarizes the computational load of the P_1 FEM and MHFEM. We averaged run-time and iteration count over all the dipole sources tested on a particular grid. We observe that solution of the MHFEM system takes roughly 15 times longer than that of the P_1 FEM. This is mainly due to the MHFEM system size which is approximately 12 times larger (ratio of the number of faces to the number of nodes in our unstructured tetrahedral grids, Table I). The AMG preconditioner performs fairly well for both FEMs, yet in the case of the MHFEM the iteration count is somewhat higher. Also, the iteration count for the fine grid is quite small (20 iterations for the P_1 FEM, 27 iterations for the MHFEM) what illustrates optimality of the applied solver.

To justify higher computational expenses of the MHFEM, we compared P_1 FEM on the refined grid versus the MHFEM on the coarse grid. From Fig. 5, we see that for EEG modeling P_1 FEM on the refined grid provides comparable or better accuracy than the MHFEM on the coarse grid. While for MEG modeling, MHFEM on the coarse grid has mainly better accuracy than P_1 FEM on the refined grid. For EEG modeling, P_1 FEM on the refined grid is faster than the MHFEM on the coarse grid. This is related to the system size (235'798 unknowns for P_1 FEM versus 350'500 unknowns MHFEM) and iteration count (23 versus 38, respectively). However, in MEG modeling, we see that the MHFEM on the coarse grid is more than an order of magnitude faster than P_1 FEM on the refined grid. This is related to the computational complexity of the Biot-Savart formula, which is proportional to the number of tetrahedrons. We resume, that the MHFEM is beneficial for MEG modeling on coarse grids both in terms of accuracy and computational expenses.

In real data processing, the transfer matrix approach [22] is typically applied to move the burden of the forward modeling from a *computational* to a *pre-computational* step. The approach is equally applicable to both P1 FEM and MHFEM discretization methods as well as to both EEG and MEG data. The CPU time at the pre-computational step can be estimated as single-source modeling time multiplied by the number of sensors. At the computational step, the CPU time is proportional to the number of sensors multiplied by the dimension of a source finite-element space. Had we chosen to apply the pre-computational step to the P1 FEM on the refined grid and the MHFEM on the coarse grid for MEG data modeling, we would have seen a dramatic difference in the CPU time in favor of the MHFEM (Table II). The difference in the pre-computational steps would have been multiplied by the number of sensors. The computational steps would have taken somewhat similar times, with some favor to P1 FEM (the respective dimensions are m_{coarse}=350'800 for MHFEM on the coarse grid and $l_{refined}$=235'798 for P1 FEM on the refined grid, Table I). Still, the MHFEM would produce more accurate MEG responses, as noted earlier (Fig 5).

We were unable to benchmark our code against the conventional mixed FEM because it would require an implementation of a separate solver. Still, some performance indicators on the mixed FEM have been published for a layered spherical head model. Thesis [23, Table 5.4] reported that the Uzawa solver for the mixed FEM system took 60 s on a cubic grid with 3'262'312 elements to achieve a tolerance of 1e-8. Our solver took 165 s for the fine tetrahedral grid with 4'927'680 elements to achieve a tolerance of 1e-10. We cannot compare these numbers directly due to differences in target tolerance, computational systems, head discretization, etc. However, considering that the Uzawa solver for the mixed FEM system can be implemented with the potential variable only, it is likely that the mixed FEM will be faster in most EEG modeling scenarios. We hope to perform a dedicated study of the two algorithms' performance in the future.

The Geselowitz formula was 27-30 times faster than Biot-Savart formula for calculation MEG responses, since the former involve integration over organ surfaces only, while the later requires integration over the whole head volume conductor. The P_1 FEM and MHFEM require roughly the same CPU time when combined with Biot-Savart or Geselowitz formulas. This computational load depends mainly on the order of quadratures used in (31), (32), (36), (37) rather than the FEM type.
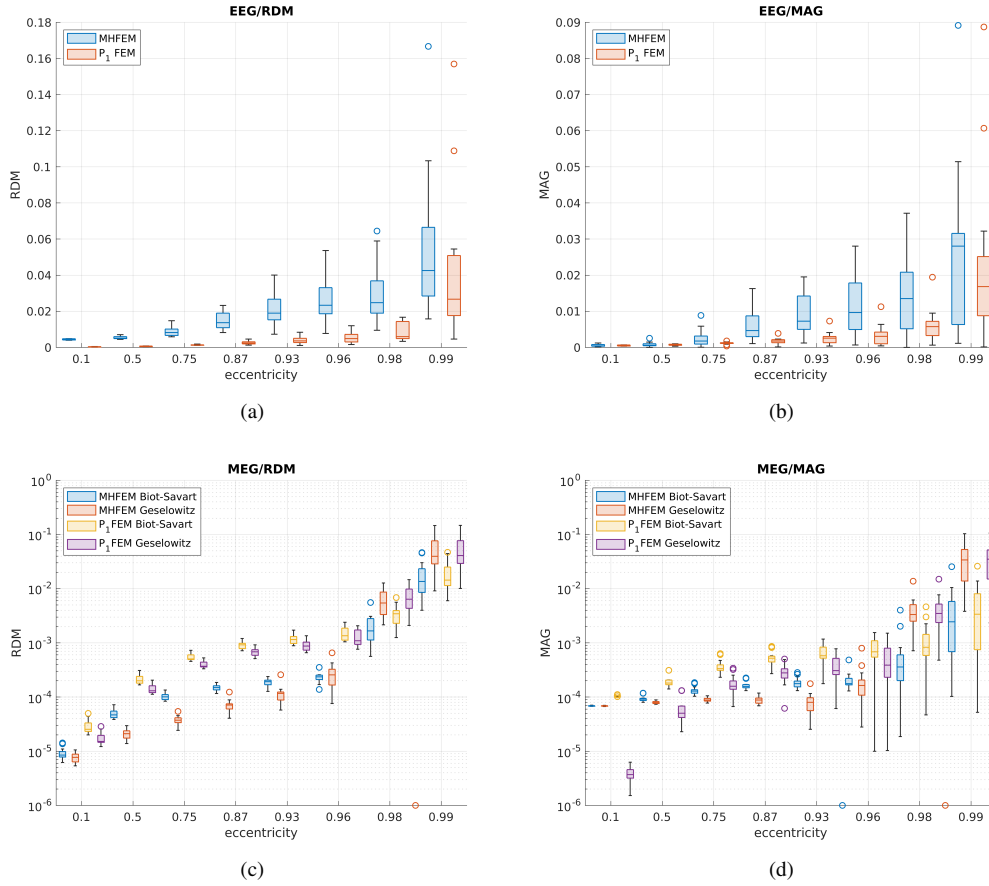
Fig. 4: RDM and MAG error boxplots of EEG and MEG data ($\boldsymbol{B}_s$) for fine grid modeling

TABLE II: Computational load of the P_1 FEM and MHFEM on the fine, coarse, and refined grids: preconditioned conjugate gradient iteration count (PCG it) and CPU time (PCG time), CPU time required by Biot-Savart and Geselowitz formula. Run-time and iteration count were averaged over all the dipole sources tested on a particular grid

grid	method	PCG it	PCG time	Biot-Savart	Geselowitz
fine	P_1FEM	20	11 s	247 s	9.1 s
fine	MHFEM	27	165 s	262 s	8.5 s
coarse	P_1FEM	20	0.2 s	13.2 s	–
coarse	MHFEM	38	3.6 s	8.4 s	–
refined	P_1FEM	23	2.3 s	104 s	–

C. EEG and MEG Data Modeling in a Real Head

In this subsection, as a proof of concept, we modeled EEG and MEG data over an anatomical head model. The 3D head model was built from T1-weighted MRI volume and was earlier described in [24]. The final tetrahedral grid consisted of four counterparts: the skin (0.43 S/m), skull (0.01 S/m), cerebrospinal fluid (1.79 S/m), and brain (0.33 S/m). The grid contained 498'876 tetrahedrons, 85'528 vertices and 1'008'022 faces (Figure 6a) and had the maximum edge length of 0.96 cm.

We modeled a dipole source located in the visual cortex (Figure 6b). The dipole was tangential to the scalp, thus the magnetic field was expected to be well-pronounced.

EEG data was collected at 129 electrode locations corresponding to GSN HydroCel-129 montage. MEG data was collected at 102 magnetometer locations corresponding to Elekta Neuromag®TRIUX™ system, Figure 6a). The magnetometers were assumed to be normal to the scalp.

Topographic EEG and MEG maps visualized in `MNE-Python` [25] are shown in Figures 7. We note that the MEG map is approximately 90° rotated relative to the EEG map, what follows form the right-hand rule.

Table III shows the computational load in this experiment. As in the above results, we see that P_1 FEM EEG modeling is much faster, while MEG modeling takes roughly the same CPU time for both FEMs.

TABLE III: Computational load of the P_1 FEM and MHFEM for real head modeling: preconditioned conjugate gradient iteration count (PCG it) and CPU time (PCG time), CPU time required by Biot-Savart and Geselowitz formula.

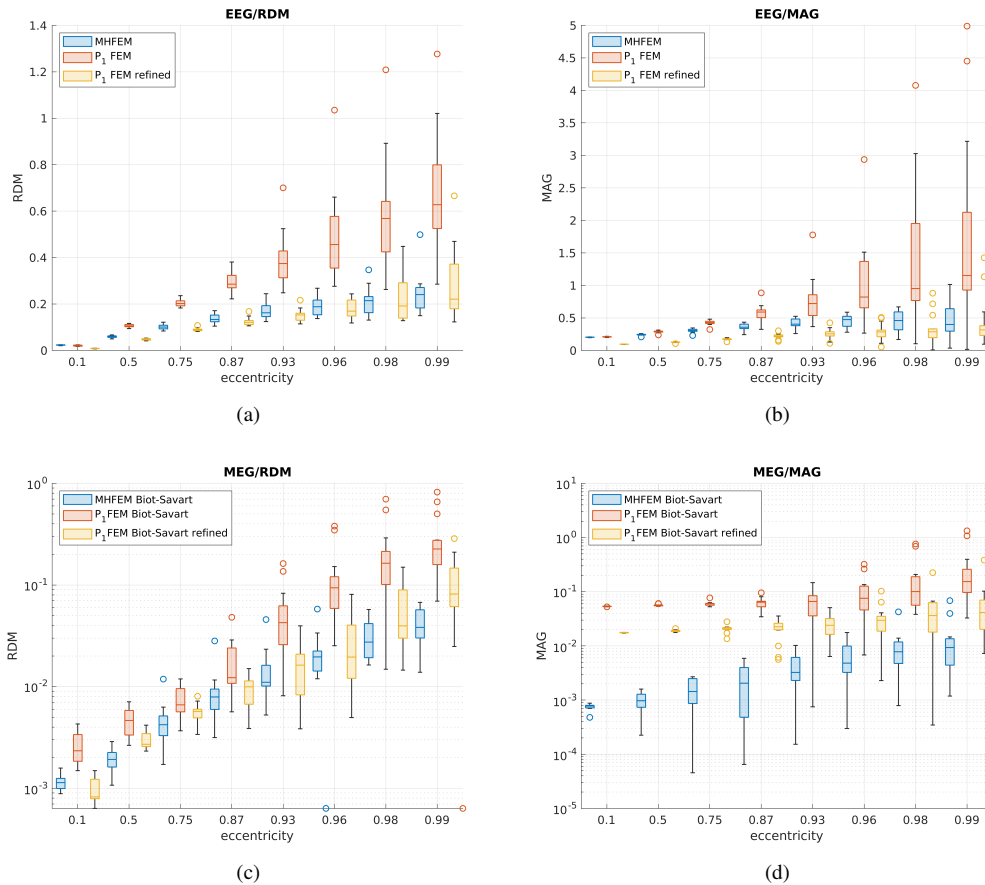| method	PCG it	PCG time	Biot-Savart	Geselowitz
P_1FEM	20	0.6 s	47 s	5.5 s
MHFEM	51	21.5 s	39 s	4.5 s

Fig. 5: RDM and MAG error boxplots of EEG and MEG data ($\boldsymbol{B}_s$) for coarse and refined grid modeling

V. DISCUSSION AND CONCLUSION

In this investigation, we introduced and assessed the MHFEM for EEG and MEG modeling on unstructured tetrahedral grids. The MHFEM provides cell-centered potential, face-centered potential through Lagrange multipliers, and normal components of the induced current at face centers. These discrete variables could be differently used to obtain EEG and MEG responses. We studied these possibilities in our work.

We compared accuracy and run-time of MHFEM and conventional P_1 FEM on fine, coarse, and realistic grids. Although run-time performance is very implementation-dependent, it gave a good indication of the computational complexity. Our experiments on EEG modeling show that the use of MHFEM is beneficial on coarse grids or low-resolution head models. In this setting due to fulfillment of the discrete charge conservation property, MHFEM accurately models induced currents. This complies with earlier works [8], [7]. AMG preconditioned conjugate gradient solver optimality was observed for the MHFEM system of equations: the iteration count even for a very large grid of almost 5 million tetrahedrons was quite moderate. As in the case of EEG modeling, MHFEM for MEG modeling is more accurate than P_1 FEM on low-resolution grids. We noticed that the Biot-Savart formula is substantially more computationally demanding than the Geselowitz formula. However, the Geselowitz formula is not

applicable on low-resolution head models. Given a particular MEG calculation formula, its run-time is of minor dependence on the FEM type.

We also made a comparison P_1 FEM modeling on the refined grid versus MHFEM on the coarse grid. For EEG modeling, P_1 FEM accuracy was improved and its computational expenses were close to those of MHFEM. While for MEG modeling, we observed that MHFEM on the coarse grid is more than an order of magnitude faster than P_1 FEM on the refined grid and also notably more accurate. We resume, that MHFEM is beneficial for MEG modeling on coarse grids both in terms of accuracy and computational expenses.

For dipole source modeling with the Biot-Savart formula, we found a new representation that involves integration of finite quantities only. It combines volume and surface integration and different from the one used in [7]. A somewhat close expression was derived in [26, (2.26)], but they preferred to perform surface integration over a small subdomain with the source. On the other hand, our expression involves surface integration over the head volume conductor boundary.

MHFEM system size is much larger than that of the conventional P_1 FEM what ultimately contributes to its solution time. We thus plan to implement shared memory parallelization to further leverage MHFEM modeling. Other future goals would be to investigate this approach for gradiometer data modeling as well as to combine it with source localization algorithms
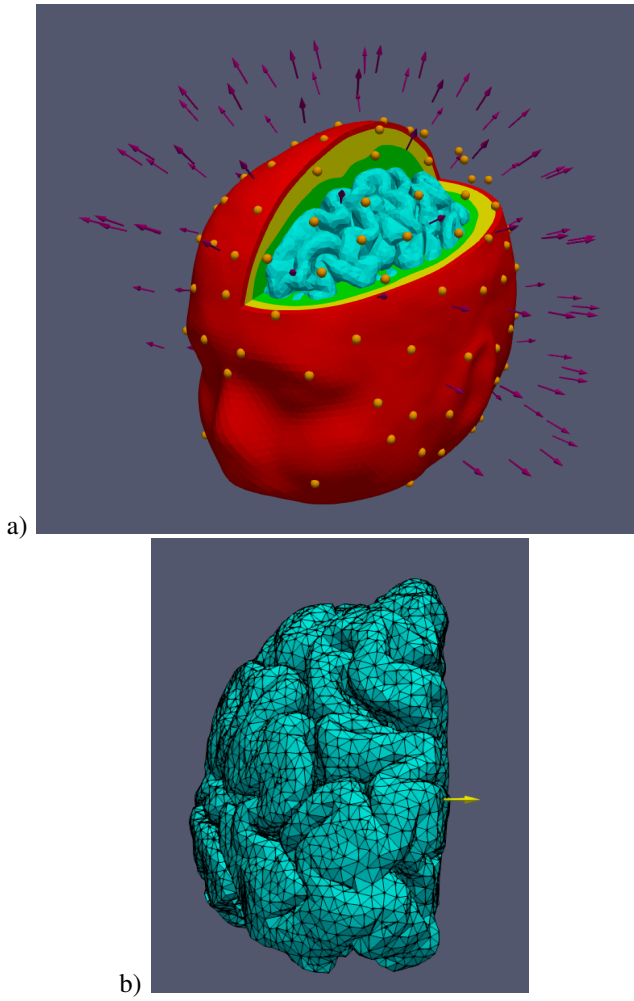
a)

b)

Fig. 6: a) Anatomical head counterparts (blue – brain, green – CSF, yellow – skull, red – scalp) and EEG (yellow balls) and MEG (violet arrows) montages. b) Dipole source (marked as arrow) located in the visual cortex of the left hemisphere

(e.g. [27]) and potential propagation methods [28]. Another application of this work is data-learned source localization [29] requiring many accurately solved forward problems.

APPENDIX

A. Reduction of MHFEM system

In this appendix, we discuss properties of the MHFEM system (13) and a procedure to transform it into a smaller system.

Note that the support of the basis functions v_i of U_h is limited to a particular tetrahedron, thus matrix A is block-diagonal with each block being 4x4 and corresponding to a particular tetrahedron. Same for matrix B: each row has four nonzero entries corresponding to a particular tetrahedron.

Practically, this means that we can eliminate u_h,

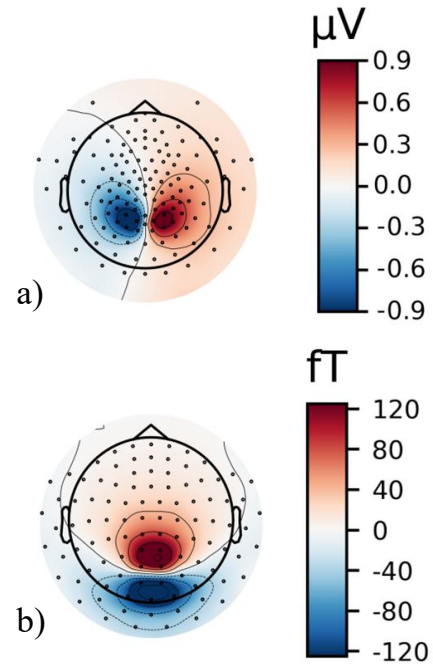$$u_h = A^{-1}(f + Bp_h - C\lambda_h), \qquad (18)$$

a)

b)

Fig. 7: Topographic EEG and MEG maps: a) piece-wise affine potential post-processed using induced currents; b) normal to the scalp magnetic flux computed with the Biot-Savart law

and receive a Schur complement system,

$$\begin{pmatrix} -B^T A^{-1} B & B^T A^{-1} C \\ C^T A^{-1} B & -C^T A^{-1} C \end{pmatrix} \begin{pmatrix} p_h \\ \lambda_h \end{pmatrix} = \begin{pmatrix} B^T A^{-1} f_h \\ -C^T A^{-1} f_h \end{pmatrix}. \qquad (19)$$

Matrix $B^T A^{-1} B$ is diagonal, we thus can continue elimination,

$$p_h = -(B^T A^{-1} B)^{-1}[B^T A^{-1} f_h - B^T A^{-1} C\lambda_h], \qquad (20)$$

and receive a system for interelement multipliers only,

$$C^T[A^{-1} - A^{-1} B(B^T A^{-1} B)^{-1} B^T A^{-1}]C\lambda_h = \\ C^T[A^{-1} - A^{-1} B(B^T A^{-1} B)^{-1} B^T A^{-1}]f_h. \qquad (21)$$

This system appeared in the text as (14). The matrix is sparse and symmetric. We can also show that it is positive semi-definite if we rewrite it as

$$S = C^T A^{-\frac{1}{2}}(I - FF^T)A^{-\frac{1}{2}}C, \qquad (22)$$

with $F = A^{-\frac{1}{2}} B(B^T A^{-1} B)^{-\frac{1}{2}}$. The expression in the middle of (22) is evidently an orthogonal projector and thus has eigenvalues 0 and 1 only. Consequently, S is positive semi-definite.

Although the expressions for the matrix and right-hand side look quite complex, we should emphasize that they could be computed in linear time. The Structure of A, B, and C allows computing local submatrices of S following formula (21) and directly assembling S from them. After λ_h is found, the potential p_h is recovered using (20) and u_h is recovered using (18).

B. Subtraction Approach for the nodal FEM

The subtraction approach is very standard for EEG FEM modeling (e.g. [30]), yet its application for MEG modeling was not commonly discussed. This appendix discusses this topic.

Consider a dipole source with moment $\boldsymbol{Q}$ located in r_0 in a subdomain with conductivity σ_p. Let p_p be a potential due to this source in a homogeneous space with conductivity σ_p,

$$-div(\sigma_p \nabla p_p) = -div\ \boldsymbol{J} \text{ in } \Omega. \tag{23}$$

The expression for p_p is well-known,

$$p_p(\boldsymbol{r}) = \frac{1}{4\pi\sigma_p} \frac{\boldsymbol{Q} \cdot (\boldsymbol{r} - \boldsymbol{r}_0)}{|\boldsymbol{r} - \boldsymbol{r}_0|^3}. \tag{24}$$

Introduce the secondary conductivity, $\sigma_s(\boldsymbol{r})$, and potential, $p_s(\boldsymbol{r})$, such that

$$\begin{aligned} \sigma(\boldsymbol{r}) &= \sigma_s(\boldsymbol{r}) + \sigma_p, \\ p(\boldsymbol{r}) &= p_p(\boldsymbol{r}) + p_s(\boldsymbol{r}). \end{aligned} \tag{25}$$

Subtraction of (23) from (1) results in,

$$-div(\sigma \nabla p_s) = div(\sigma_s \nabla p_p) \text{ in } \Omega. \tag{26}$$

which is an equation for the secondary potential. Boundary conditions could be easily derived as well,

$$\sigma \frac{\partial p_s}{\partial \boldsymbol{\nu}} = -\sigma \frac{\partial p_p}{\partial \boldsymbol{\nu}} \text{ on } \Gamma. \tag{27}$$

We refer to [30] for further discussion on the subtraction method for EEG modeling. Let us now discuss computation of the MEG response.

From (3), we have,

$$\begin{aligned} \boldsymbol{B}_s(r) = &-\frac{\mu_0}{4\pi}\sigma_p \int_\Omega \nabla p \times \frac{\boldsymbol{r} - \boldsymbol{r}'}{|\boldsymbol{r} - \boldsymbol{r}'|^3} dV' \\ &-\frac{\mu_0}{4\pi} \int_\Omega \sigma_s \nabla p \times \frac{\boldsymbol{r} - \boldsymbol{r}'}{|\boldsymbol{r} - \boldsymbol{r}'|^3} dV'. \end{aligned} \tag{28}$$

The integrand of the first term is singular at the dipole location. We thus preferred to rewrite it as,

$$-\frac{\mu_0}{4\pi}\sigma_p \int_\Omega curl \left(p \frac{\boldsymbol{r} - \boldsymbol{r}'}{|\boldsymbol{r} - \boldsymbol{r}'|^3} \right) dV', \tag{29}$$

which can expressed as a surface integral,

$$\frac{\mu_0}{4\pi}\sigma_p \int_\Gamma p \frac{\boldsymbol{r} - \boldsymbol{r}'}{|\boldsymbol{r} - \boldsymbol{r}'|^3} \times \boldsymbol{\nu}\ dS' \tag{30}$$

Substituting $p = p_p + p_s$, we thus end up with,

$$\begin{aligned} \boldsymbol{B}_s(\boldsymbol{r}) = &\frac{\mu_0}{4\pi}\sigma_p \int_\Gamma (p_p + p_s) \frac{\boldsymbol{r} - \boldsymbol{r}'}{|\boldsymbol{r} - \boldsymbol{r}'|^3} \times \boldsymbol{\nu}\ dS' \\ &+\frac{\mu_0}{4\pi} \int_\Omega \sigma_s(\nabla p_p + \nabla p_s) \times \frac{\boldsymbol{r} - \boldsymbol{r}'}{|\boldsymbol{r} - \boldsymbol{r}'|^3} dV'. \end{aligned} \tag{31}$$

We emphasize that $p_s\ \nabla p_s$ are bounded within the modeling domain. Also, $\sigma_s \nabla p_p$ is bounded since σ_s vanishes at the dipole location. p_p is bounded on Γ that is why computations using the above formula involve only finite quantities (see the discussion in [7] for comparison).

The Geselowitz formula in this setting takes the form,

$$\boldsymbol{B}_s(r) = \frac{\mu_0}{4\pi} \sum_{j=1}^M (\sigma'_j - \sigma''_j) \int_{S_j} (p_p + p_s) \frac{\boldsymbol{r} - \boldsymbol{r}'}{|\boldsymbol{r} - \boldsymbol{r}'|^3} \times \boldsymbol{\nu} dS'. \tag{32}$$

C. Subtraction Approach for the MHFEM

In this appendix, we discuss incorporation of the subtraction approach into the MHFEM.

The mixed formulation of (26), (27) that we utilized in this work is the following,

$$\begin{aligned} \frac{1}{\sigma}\boldsymbol{u}_s + \nabla p_s &= -\frac{\sigma_s}{\sigma}\nabla p_p, \\ -div\ \boldsymbol{u}_s &= 0. \end{aligned} \tag{33}$$

completed with

$$\boldsymbol{u}_s \cdot \boldsymbol{\nu} = \sigma_b \frac{\partial p_p}{\partial \boldsymbol{\nu}} \text{ on } \Gamma, \tag{34}$$

i.e. $\boldsymbol{u}_s = -\sigma \nabla p_s - \sigma_s \nabla p_p$.

After solving the respective discrete system of equations we receive an approximation to $(\boldsymbol{u}_s, p_s, \lambda_s)$.

Now EEG response is given by substituting p_s into (25), while by substituting $\boldsymbol{u}_s$ in (15), we find the next way to compute the magnetic field,

$$\begin{aligned} \boldsymbol{B}_s(\boldsymbol{r}) = &-\frac{\mu_0}{4\pi}\sigma_p \int_\Omega \nabla p_p \times \frac{\boldsymbol{r} - \boldsymbol{r}'}{|\boldsymbol{r} - \boldsymbol{r}'|^3} dV' \\ &+\frac{\mu_0}{4\pi} \int_\Omega \boldsymbol{u}_s \times \frac{\boldsymbol{r} - \boldsymbol{r}'}{|\boldsymbol{r} - \boldsymbol{r}'|^3} dV'. \end{aligned} \tag{35}$$

As in Appendix B, we can avoid volume integration of the unbound term ∇p_p and express it as a surface integral. This ultimately results in the following expression for $\boldsymbol{B}_s$,

$$\begin{aligned} \boldsymbol{B}_s(\boldsymbol{r}) = &\frac{\mu_0}{4\pi}\sigma_p \int_\Gamma p_p \frac{\boldsymbol{r} - \boldsymbol{r}'}{|\boldsymbol{r} - \boldsymbol{r}'|^3} \times \boldsymbol{\nu}\ dS' \\ &+\frac{\mu_0}{4\pi} \int_\Omega \boldsymbol{u}_s \times \frac{\boldsymbol{r} - \boldsymbol{r}'}{|\boldsymbol{r} - \boldsymbol{r}'|^3} dV'. \end{aligned} \tag{36}$$

The Geselowitz formula (16) now takes the form,

$$\boldsymbol{B}_s(r) = \frac{\mu_0}{4\pi} \sum_{j=1}^M (\sigma'_j - \sigma''_j) \int_{S_j} (p_p + \lambda_s) \frac{\boldsymbol{r} - \boldsymbol{r}'}{|\boldsymbol{r} - \boldsymbol{r}'|^3} \times \boldsymbol{\nu} dS'. \tag{37}$$

ACKNOWLEDGMENT

REFERENCES

[1] J. Sarvas, "Basic mathematical and electromagnetic concepts of the biomagnetic inverse problem," *Physics in Medicine and Biology*, vol. 32, no. 1, pp. 11–22, jan 1987.

[2] Y. Yan, P. L. Nunez, and R. T. Hart, "Finite-element model of the human head: scalp potentials due to dipole sources," *Medical & Biological Engineering & Computing*, vol. 29, no. 5, pp. 475–481, Sep. 1991. [Online]. Available: https://doi.org/10.1007/bf02442317

[3] G. Marin, C. Guerin, S. Baillet, L. Garnero, and G. Meunier, "Influence of skull anisotropy for the forward and inverse problem in EEG: Simulation studies using FEM on realistic head models," *Human Brain Mapping*, vol. 6, no. 4, pp. 250–269, 1998. [Online]. Available: https://doi.org/10.1002/(sici)1097-0193(1998)6:4¡250::aid-hbm5¿3.0.co;2-2

[4] S. Lew, C. Wolters, T. Dierkes, C. Rer, and R. MacLeod, "Accuracy and run-time comparison for different potential approaches and iterative solvers in finite element method based eeg source analysis," *Applied Numerical Mathematics*, vol. 59, no. 8, pp. 1970 – 1988, 2009. [Online]. Available: http://www.sciencedirect.com/science/article/pii/S016892740900021X

[5] R. Eymard, T. Gallouet, and R. Herbin, "Finite volume methods," in *Handbook of Numerical Analysis*. Elsevier, 2000, pp. 713–1018. [Online]. Available: https://doi.org/10.1016/s1570-8659(00)07005-8

[6] D. A. D. Pietro and A. Ern, *Mathematical Aspects of Discontinuous Galerkin Methods*. Springer Berlin Heidelberg, 2012. [Online]. Available: https://doi.org/10.1007/978-3-642-22980-0

[7] M. C. Piastra, A. Nüßing, J. Vorwerk, H. Bornfleth, R. Oostenveld, C. Engwer, and C. H. Wolters, "The discontinuous galerkin finite element method for solving the meg and the combined meg/eeg forward problem," *Frontiers in Neuroscience*, vol. 12, p. 30, 2018. [Online]. Available: https://www.frontiersin.org/article/10.3389/fnins.2018.00030

[8] C. Engwer, J. Vorwerk, J. Ludewig, and C. H. Wolters, "A discontinuous galerkin method to solve the eeg forward problem using the subtraction approach," *SIAM Journal on Scientific Computing*, vol. 39, no. 1, pp. B138–B164, 2017. [Online]. Available: https://doi.org/10.1137/15M1048392

[9] F. Brezzi and M. Fortin, *Mixed and Hybrid Finite Element Methods*. Springer, 1991.

[10] D. Braess, *Finite Elements: Theory, Fast Solvers, and Applications in Elasticity Theory*. Cambridge University Press, 2007.

[11] J. Vorwerk, C. Engwer, S. Pursiainen, and C. H. Wolters, "A mixed finite element method to solve the eeg forward problem," *IEEE Transactions on Medical Imaging*, vol. 36, no. 4, pp. 930–941, April 2017.

[12] E. Bigler, *Neuroimaging I: Basic Science*, ser. Human Brain Function: Assessment and Rehabilitation. Springer US, 1996.

[13] I. G. Gjerde, K. Kumar, and J. M. Nordbotten, "A singularity removal method for coupled 1d–3d flow models," *Computational Geosciences*, vol. 24, no. 2, pp. 443–457, Dec. 2019. [Online]. Available: https://doi.org/10.1007/s10596-019-09899-4

[14] P. A. Raviart and J. M. Thomas, "A mixed finite element method for 2-nd order elliptic problems," in *Mathematical Aspects of Finite Element Methods*, A. Dold and B. Eckmann, Eds. Springer, 1977, lecture Notes of Mathematics, Volume 606.

[15] V. E. Henson and U. M. Yang, "Boomeramg: A parallel algebraic multigrid solver and preconditioner," *Applied Numerical Mathematics*, vol. 41, no. 1, pp. 155 – 177, 2002, developments and Trends in Iterative Methods for Large Systems of Equations - in memorium Rudiger Weiss.

[16] R. Anderson, J. Andrej, A. Barker, J. Bramwell, J.-S. Camier, J. C. V. Dobrev, Y. Dudouit, A. Fisher, T. Kolev, W. Pazner, M. Stowell, V. Tomov, I. Akkerman, J. Dahm, D. Medina, and S. Zampini, "MFEM: A modular finite element library," *Computers & Mathematics with Applications*, 2020.

[17] Qianqian Fang and D. A. Boas, "Tetrahedral mesh generation from volumetric binary and grayscale images," in *2009 IEEE International Symposium on Biomedical Imaging: From Nano to Macro*, 2009, pp. 1142–1145.

[18] I. Despotović, B. Goossens, and W. Philips, "Mri segmentation of the human brain: challenges, methods, and applications," *Computational and mathematical methods in medicine*, vol. 2015, 2015.

[19] S. Næss, C. Chintaluri, T. V. Ness, A. M. Dale, G. T. Einevoll, and D. K. Wójcik, "Corrected four-sphere head model for eeg signals," *Frontiers in human neuroscience*, vol. 11, p. 490, 2017. [Online]. Available: https://europepmc.org/articles/PMC5651266

[20] F. Drechsler, C. Wolters, T. Dierkes, H. Si, and L. Grasedyck, "A full subtraction approach for finite element method based source analysis using constrained delaunay tetrahedralisation," *NeuroImage*, vol. 46, no. 4, pp. 1055 – 1065, 2009. [Online]. Available: http://www.sciencedirect.com/science/article/pii/S1053811909001761

[21] J. Kybic, M. Clerc, T. Abboud, O. Faugeras, R. Keriven, and T. Papadopoulo, "A common formalism for the integral formulations of the forward eeg problem," *IEEE Transactions on Medical Imaging*, vol. 24, no. 1, pp. 12–28, 2005.

[22] J. C. de Munck, C. H. Wolters, and M. Clerc, *EEG and MEG: forward modeling*. Cambridge University Press, 2012, pp. 192–256.

[23] J. Vorwerk, "New finite element methods to solve the eeg/meg forward problem," Ph.D. dissertation, Westfälische Wilhelms-Universität Münster, 2016.

[24] M. Malovichko, N. Koshev, N. Yavich, A. Razorenova, and M. Fedorov, "Electroencephalographic source reconstruction by the finite-element approximation of the elliptic cauchy problem," *IEEE Transactions on Biomedical Engineering*, pp. 1–1, 2020. [Online]. Available: https://doi.org/10.1109/tbme.2020.3021359

[25] A. Gramfort, M. Luessi, E. Larson, D. Engemann, D. Strohmeier, C. Brodbeck, R. Goj, M. Jas, T. Brooks, L. Parkkonen, and M. Hämäläinen, "Meg and eeg data analysis with mne-python," *Frontiers in Neuroscience*, vol. 7, p. 267, 2013.

[26] M. C. Piastra, "New finite element methods for solving the meg and the combined meg/eeg forward problem," Ph.D. dissertation, University of Münster, 2019. [Online]. Available: http://nbn-resolving.de/urn:nbn:de:hbz:6-53199662090

[27] F.-H. Lin, T. Witzel, S. P. Ahlfors, S. M. Stufflebeam, J. W. Belliveau, and M. S. Hämäläinen, "Assessing and improving the spatial accuracy in MEG source localization by depth-weighted minimum-norm estimates," *NeuroImage*, vol. 31, no. 1, pp. 160–171, May 2006. [Online]. Available: https://doi.org/10.1016/j.neuroimage.2005.11.054

[28] N. Koshev, N. Yavich, M. Malovichko, E. Skidchenko, and M. Fedorov, "Fem-based scalp-to-cortex eeg data mapping via the solution of the cauchy problem," *Journal of Inverse and Ill-posed Problems*, vol. 28, no. 4, pp. 517 – 532, 01 Aug. 2020. [Online]. Available: https://www.degruyter.com/view/journals/jiip/28/4/article-p517.xml

[29] A. Razorenova, N. Yavich, M. Malovichko, M. Fedorov, N. Koshev, and D. V. Dylov, "Deep learning for non-invasive cortical potential imaging," in *Machine Learning in Clinical Neuroimaging and Radiogenomics in Neuro-oncology*. Cham: Springer International Publishing, 2020, pp. 45–55.

[30] C. Wolters, H. Köstler, C. Möller, J. Härdtlein, L. Grasedyck, and W. Hackbusch, "Numerical mathematics of the subtraction method for the modeling of a current dipole in eeg source reconstruction using finite element head models," *SIAM J. Sci. Comput.*, vol. 30, pp. 24–45, 2007.

[31] I. Zacharov, R. Arslanov, M. Gunin, D. Stefonishin, A. Bykov, S. Pavlov, O. Panarin, A. Maliutin, S. Rykovanov, and M. Fedorov, "Zhores — petaflops supercomputer for data-driven modeling, machine learning and artificial intelligence installed in skolkovo institute of science and technology," *Open Engineering*, vol. 9, no. 1, pp. 512 – 520, 2019. [Online]. Available: https://www.degruyter.com/view/journals/eng/9/1/article-p512.xml